The Astrophysical Journal Letters, 937:L1 (11pp), 2022 September 20 https://doi.org/10.3847/2041-8213/ac8b10

ALMA Detection of Dust Trapping around Lagrangian Points in the LkCa 15 Disk

Feng Long (龙凤)[1], Sean M. Andrews[1], Shangjia Zhang (张尚嘉)[2], Chunhua Qi[1], Myriam Benisty[3,4], Stefano Facchini[5], Andrea Isella[6], David J. Wilner[1], Jaehan Bae[7], Jane Huang[8,10], Ryan A. Loomis[9], Karin I. Öberg[1], and Zhaohuan Zhu (朱照寰)[2]
[1] Center for Astrophysics | Harvard & Smithsonian, 60 Garden Street, Cambridge, MA 02138, USA; feng.long@cfa.harvard.edu
[2] Department of Physics and Astronomy, University of Nevada, Las Vegas, 4505 S. Maryland Parkway, Las Vegas, NV 89154, USA
[3] Univ. Grenoble Alpes, CNRS, IPAG, F-38000 Grenoble, France
[4] Université Côte d'Azur, Observatoire de la Côte d'Azur, CNRS, Laboratoire Lagrange, France
[5] Università degli Studi di Milano, via Giovanni Celoria 16, I-20133 Milano, Italy
[6] Department of Physics and Astronomy, Rice University, 6100 Main Street, MS-108, Houston, TX 77005, USA
[7] Department of Astronomy, University of Florida, Gainesville, FL 32611, USA
[8] Department of Astronomy, University of Michigan, 323 West Hall, 1085 S. University Avenue, Ann Arbor, MI 48109, USA
[9] National Radio Astronomy Observatory, 520 Edgemont Road, Charlottesville, VA 22903, USA
Received 2022 July 11; revised 2022 August 9; accepted 2022 August 15; published 2022 September 14

Abstract

We present deep high-resolution (∼50 mas, 8 au) Atacama Large Millimeter/submillimeter Array (ALMA) 0.88 and 1.3 mm continuum observations of the LkCa 15 disk. The emission morphology shows an inner cavity and three dust rings at both wavelengths, but with slightly narrower rings at the longer wavelength. Along a faint ring at 42 au, we identify two excess emission features at $\sim 10\sigma$ significance at both wavelengths: one as an unresolved clump and the other as an extended arc, separated by roughly 120° in azimuth. The clump is unlikely to be a circumplanetary disk (CPD) as the emission peak shifts between the two wavelengths even after accounting for orbital motion. Instead, the morphology of the 42 au ring strongly resembles the characteristic horseshoe orbit produced in planet–disk interaction models, where the clump and the arc trace dust accumulation around Lagrangian points L_4 and L_5, respectively. The shape of the 42 au ring, dust trapping in the outer adjacent ring, and the coincidence of the horseshoe ring location with a gap in near-IR scattered light, are all consistent with the scenario of planet sculpting, with the planet likely having a mass between those of Neptune and Saturn. We do not detect pointlike emission associated with a CPD around the putative planet location (0.″27 in projected separation from the central star at a position angle of ∼60°), with upper limits of 70 and 33 μJy at 0.88 and 1.3 mm, respectively, corresponding to dust mass upper limits of 0.02–0.03 $M_\oplus$.

Unified Astronomy Thesaurus concepts: Planetary-disk interactions (2204); Protoplanetary disks (1300); Exoplanet formation (492)

1. Introduction

Disk substructures, in the forms of gaps and rings, spiral arms, and asymmetries, are prevalent in high angular resolution images from both millimeter continuum emission and optical/near-infrared scattered light (see recent reviews by Andrews 2020; Benisty et al. 2022). These features are widely taken as the imprints of planet–disk interactions (e.g., Zhu et al. 2011; Pinilla et al. 2012; Dipierro et al. 2015), predicting a wealth of young planets with masses of 0.1–1 $M_{\rm Jup}$ at orbital distances of 10–100 au (e.g., Bae et al. 2018; Zhang et al. 2018; Lodato et al. 2019). However, confirming the presence of these planets remains challenging, as the current detection limits from direct imaging surveys are on the order of a few Jupiter masses (e.g., Asensio-Torres et al. 2021). Only in very few cases have protoplanet detections been reported (e.g., Keppler et al. 2018; Currie et al. 2022), which is consistent with the picture that most planetary perturbers are in the low-mass regime (see also Brittain et al. 2020 for an alternative explanation).

Given the challenges of directly detecting young planet photospheres, efforts from various indirect avenues are essential to confirm the planet origin of disk substructures. One recent advance is the detection of localized velocity deviations from Keplerian motion in the gas disk, where the perturbation amplitude is linked to the planet mass (Pinte et al. 2022). Another option aims to probe disk material that feeds the growth of a planet through a circumplanetary disk (CPD), on scales smaller than the Hill radius. Deep high-resolution millimeter observations could reveal such faint and compact CPDs, as have been demonstrated by the recent CPD detection around PDS 70 c (Isella et al. 2019; Benisty et al. 2021) and a new candidate in the AS 209 disk (Bae et al. 2022). A third, rarely explored, feature of planet–disk interactions is the accumulation of disk material around Lagrangian points along the planet orbit (e.g., Lyra et al. 2009; Montesinos et al. 2020). For example, the one-sided crescent-shaped asymmetry in the HD 163296 disk has been suggested to mimic dust trapping in the Lagrangian point L_5 (Rodenkirch et al. 2021).

We focus a search for evidence of these planet–disk interaction features in the continuum emission here on the LkCa 15 system. LkCa 15 is a K5 star with a mass of $1.2 \pm 0.1\,M_\odot$, located in the Taurus star-forming region at a distance of 159 pc (Gaia Collaboration et al. 2018; Donati et al. 2019). Early millimeter observations reported a dust-depleted cavity in the disk (out to a radius of ∼45 au; Piétu et al. 2006;

[10] NASA Hubble Fellowship Program Sagan Fellow.

Table 1
ALMA Observation Summary

Program ID	PI	Obs. Freq. (GHz)	UTC Time	N_{ant}	Baseline (meter)	On-source Time (min)	Ref. Ant
(1)	(2)	(3)	(4)	(5)	(6)	(7)	(8)
			Band 6 Observations				
2015.1.00118.S	L. Looney	223.06–242.93	2017 July 09-12:08	40	16-2647	12	DA62
2015.1.00118.S	L. Looney	223.06–242.93	2017 July 09-13:31	40	16-2647	12	DA62
2015.1.00118.S	L. Looney	223.06–242.93	2017 July 09-14:43	40	16-2647	12	DA62
2015.1.00118.S	L. Looney	223.06–242.93	2017 July 09-15:53	40	16-2647	12	DA62
2018.1.00945.S	C. Qi	217.06–235.43	2018 Oct 26-04:53	49	15-1397	27	DA43
2018.1.00945.S	C. Qi	217.06–235.43	2018 Nov 17-03:55	46	15-1397	27	DA43
2018.1.00945.S	C. Qi	217.06–235.43	2019 July 07-12:55	45	149-13894	29	DV09
2018.1.00945.S	C. Qi	217.06–235.43	2019 July 07-13:56	45	149-13894	29	DV09
2018.1.01255.S	M. Benisty	213.06–229.93	2019 July 13-15:23	40	111-12644	35	DV09
2018.1.01255.S	M. Benisty	213.06–229.93	2019 July 19-14:48	43	95-8547	35	DV09
2018.1.01255.S	M. Benisty	213.07–229.94	2021 Aug 20-11:28	45	59-9933	35	DA60
			Band 7 Observations				
2012.1.00870.S	L. Perez	339.09–342.96	2014 Aug 29-09:44	36	33-1090	35	DA63
2018.1.00350.S	A. Isella	332.86–348.74	2019 July 21-11:23	44	92-8547	39	DV05
2018.1.00350.S	A. Isella	332.86–348.74	2019 July 28-11:06	42	92-8547	39	DV05
2018.1.00350.S	A. Isella	332.86–348.74	2019 July 30-10:21	46	92-8547	39	DA52
2018.1.00350.S	A. Isella	332.86–348.74	2019 July 30-11:51	46	92-8547	39	DA52

Note. Column (1): ALMA program ID. Column (2): PI of the ALMA project. Column (3): frequency range used in the combined data set. Column (4): UTC time at the start of the observation. Column (5): number of antennas. Column (6): minimum and maximum baseline lengths. Column (7): on-source observing time. Column (8): reference antenna used in data calibration.

Andrews et al. 2011), making it a popular target for young planet searches. With high-resolution (68×47 mas) Atacama Large Millimeter/submillimeter Array (ALMA) observations at 1.3 mm, Facchini et al. (2020) showed that the disk has three dust rings exterior to the cavity and suggested that a planet is forming around the bright middle ring. Three giant planet candidates have also been claimed through optical and IR imaging techniques at radial distances of $0\farcs10-0\farcs13$ (16–21 au; Kraus & Ireland 2012; Sallum et al. 2015), which, however, have been later interpreted as inner disk emission (Thalmann et al. 2016; Currie et al. 2019; Blakely et al. 2022). No CPDs associated with these candidates were detected in 7 mm continuum (Isella et al. 2014).

In this Letter, we combine the long-baseline data presented in Facchini et al. (2020) with new observations and report the discovery of two excess emission features along the faintest ring in the LkCa 15 disk. Those features resemble the scenario of dust trapping in the L_4 and L_5 Lagrangian points around an unseen planet at a semimajor orbital radius of 42 au. We present ALMA observations and the details of data reduction in Section 2. The overall dust emission morphology and the new finding of significant excess emission along one dust ring are reported in Section 3. We then discuss these results in the context of planet formation in Section 4 and summarize in Section 5.

2. Observations and Data Reduction

Our analysis included ALMA continuum data with both the Band 6 (B6) and Band 7 (B7) receivers. A summary of the observations and instrument configurations is provided in Table 1. For individual executions, calibration scripts provided by the observatory were used with the specified `CASA` versions (McMullin et al. 2007) to flag problematic data, correct for bandpass responses, set absolute flux scales, and solve for complex gain variations. Self-calibration and imaging were then performed with `CASA 6.4.0`. Before concatenating data taken at different epochs, we shifted all measurement sets to a common phase center. To do so, we first created a continuum image for each data set and then determined the disk emission center in the image plane. For short-baseline data, the disk center was estimated by fitting a 2D Gaussian model with `imfit`. For long-baseline data, we applied an ellipse model to the prominent dust ring at 69 au (see Section 3) and adopted its centroid as the disk center. The `phasevis` and `fixplanets` tasks in `CASA` were then used to implement these shifts.

Self-calibration was done separately for each band, starting from the concatenated short-baseline data sets. The initial model was created with the `multiscale` algorithm implemented in the `tclean` task and a Briggs weighting parameter of 0.5. After two rounds of phase (solutions on scan-length and 60 s) and one round of amplitude self-calibration (on a scan-length interval), the peak signal-to-noise ratio (S/N) in the image was nearly doubled. The improvement for image quality was minimal for self-calibrating the combined data (including long baselines). One subsequent iteration of phase self-calibration was performed with a solution interval of 900 s and spectral windows combined.

In synthesizing a B6 continuum image, we found a good compromise between resolution and sensitivity was reached with `robust = 0` in the Briggs weighting scheme, resulting in a beam of 47×34 mas (PA $= -3\fdg3$). As discussed in Jorsater & van Moorsel (1995), the mismatch in units between CLEAN residual map (Jy per dirty beam) and the convolved CLEAN model image (Jy per clean beam) would lead to inaccurate source flux and misrepresentation of faint emission. Following the procedure outlined in Czekala et al. (2021), we rescaled the clean image residuals by the ratio of the clean and dirty beam

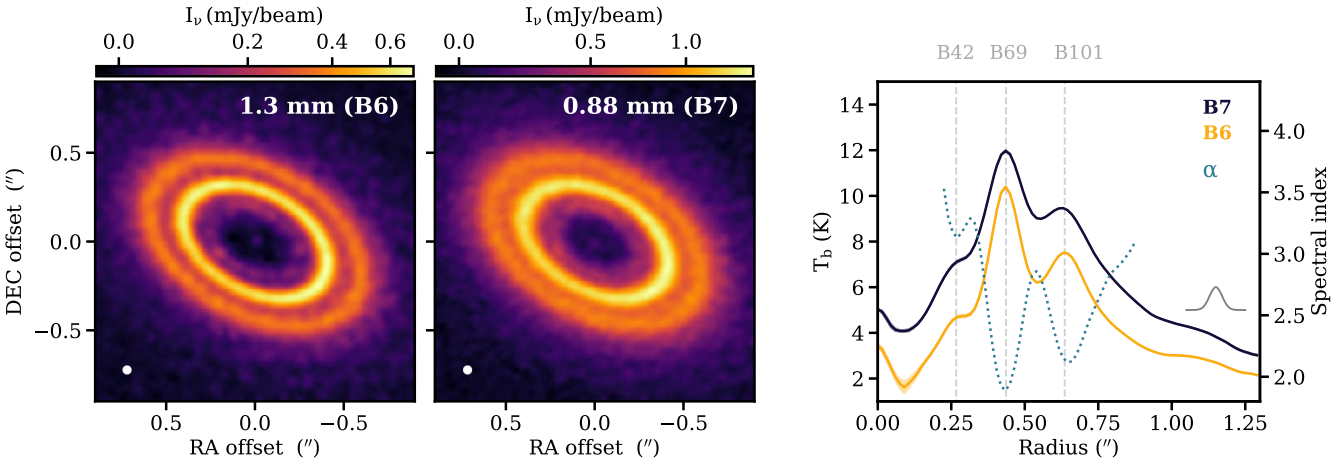

Figure 1. Left and middle: continuum emission images of the LkCa 15 disk at 1.3 and 0.88 mm, respectively, with identical beam size of 50 mas, shown in the bottom left corner of each panel. An asinh color stretch is applied to highlight the faint emission. Right: azimuthally averaged radial intensity profiles in brightness temperature. The three prominent dust rings are marked by the dashed vertical lines. The spectral index profile between the two bands is indicated by the dotted line (*y*-axis labels on the right side). The Gaussian profile in the bottom right corner shows the FWHM of the synthesized beam.

areas ($\epsilon = 0.45$) before adding to the convolved model. This effectively reduces the image noise level to 4.4 μJy beam^{-1}.[11] We note that the main results are not affected by this correction and the detection significance from the original image is discussed accordingly.

A high-resolution B7 continuum image with a beam size of 46×38 mas (PA $= 51.^{\circ}3$) was produced with a Briggs weighting of `robust = 0` and a Gaussian uvtaper (10×40 mas, 0°) using `tclean`. After correcting for the unit mismatch with $\epsilon = 0.72$, the rms noise level for the B7 continuum image was 15.5 μJy beam^{-1}. As a last step, we convolved the final images with an elliptical Gaussian kernel so they both have a circular beam with an FWHM of 50 mas (8 au). This ensures a fair comparison between the two wavelengths.

3. The Dust Disk of LkCa 15

3.1. Overall Dust Emission Morphology in LkCa 15

Figure 1 presents the new deep continuum images of the LkCa 15 disk at both 1.3 mm (B6) and 0.88 mm (B7), as well as the corresponding azimuthally averaged radial profiles, deprojected with an inclination angle of $50.^{\circ}2$ and position angle of $61.^{\circ}9$ (counting from N to E; Facchini et al. 2020). The emission morphologies at the two wavelengths are very similar, though the emission at 1.3 mm exhibits higher contrasts. The disk shows a faint inner component, a wide cavity, three dust rings spanning 0.″2–0.″8, and an outer tail extending beyond ∼1″. `CASA imfit` suggests the inner disk component is unresolved (<4 au in radius), with a spectral index of 2.4 ± 0.3 based on peak intensities of 58.6 ± 4.1 and 155.8 ± 7.9 μJy beam^{-1} at B6 and B7, respectively. Around the radial distances of the three proposed giant planet candidates (0.″10–0.″13; Kraus & Ireland 2012; Sallum et al. 2015), we do not find any significant continuum emission.

There are three dust rings peaking at 42, 69, and 101 au (hereafter B42, B69, and B101), respectively, with widths comparable to the beam size (based on the model fitting described below). The B42 ring corresponds to the emission "shoulder" reported in Facchini et al. (2020), which is better resolved in the data presented here. The two bright dust rings B69 and B101 appear to be narrower (by $\gtrsim$20% in width; see Table 2 in Appendix A) at 1.3 mm compared to 0.88 mm, which suggests that dust grains are likely trapped in local pressure bumps with larger grains being more effectively concentrated (Pinilla et al. 2015; Long et al. 2020). We obtained a spectral index map from the images at the two bands as $\alpha_{\rm mm} = \log(I_{B6}/I_{B7})/\log(\nu_{B6}/\nu_{B7})$. The radial profile of $\alpha_{\rm mm}$ (the right panel of Figure 1) reaches local minima at ring peaks and maxima in gaps. Inferring the grain properties in B69 and B101 rings is challenging because the dust emission is likely optically thick (with low $\alpha_{\rm mm} \sim 2$). The overall higher $\alpha_{\rm mm}$ around B42, however, suggests that grain properties there might be different from the outer bright disk regions.

3.2. Asymmetric Features in the B42 Ring

The innermost faint ring, B42, exhibits azimuthal asymmetries, which are better visualized in the two-wavelength combined image (at 1.1 mm) in Figure 2. That image was constructed with `robust = −0.2` in `tclean` using the `mtmfs` algorithm (Rau & Cornwell 2011) and `nterms = 2` to obtain a high angular resolution of 39×28 mas. Using an azimuthal intensity profile around this ring (made with a radial average from 0.″26 to 0.″28 in the disk plane), we identified two prominent features that are separated by ∼120° (see the bottom panel of Figure 2). We refer to these features as "clump" and "arc" based on the apparent differences in their azimuthal extensions. The clump and arc are brighter than the average of the B42 ring by about a factor of 2.

To better characterize these nonaxisymmetric features, we first built an azimuthally symmetric disk model and then analyzed a residual map where that symmetric emission was removed. This was achieved by fitting the real component of the visibilities with the `frank` software package (Jennings et al. 2020) and subtracting the model from the data to create a set of residual visibilities, from which a residual map was then produced with `tclean` (hereafter referred as "residual" throughout the Letter). This procedure has been well established in previous studies (e.g., Andrews et al. 2021; Jennings et al. 2022). We set the `frank` hyperparameters to $R_{\rm out} = 3''$ (to encompass all the

[11] The threshold in `tclean` was set to 25 and 50 μJy in B6 and B7, respectively. Compared to Facchini et al. (2020), the combined data in this study are more sensitive by a factor of ∼1.5 and reach a better angular resolution by 30%.

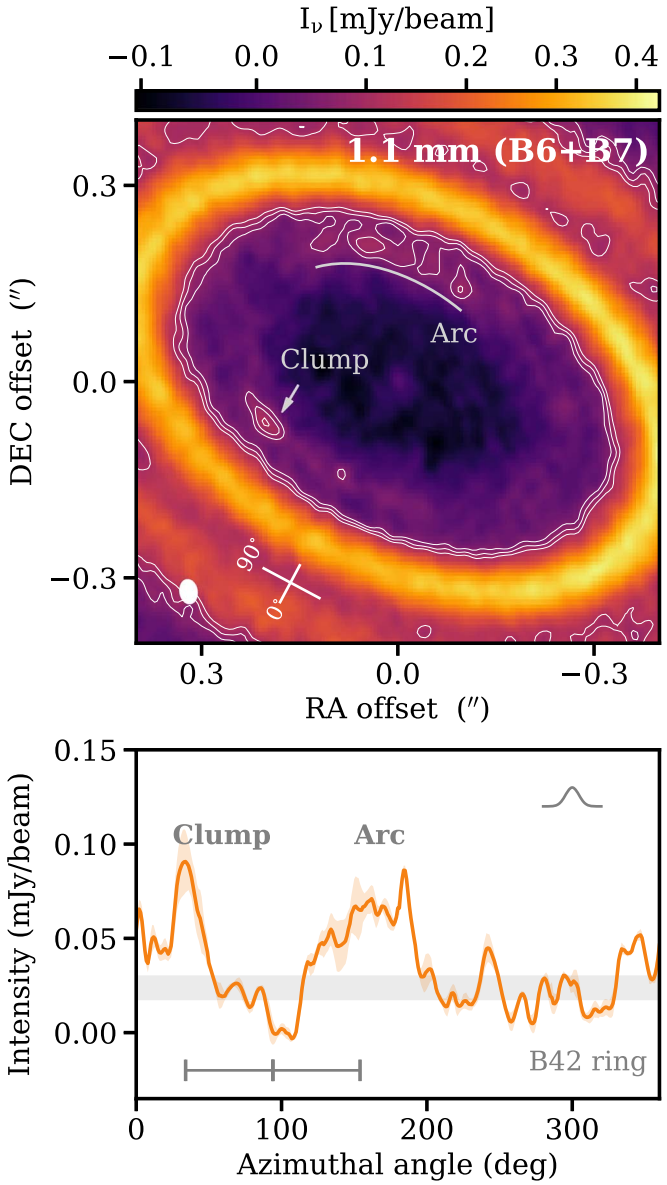

Figure 2. Top: continuum image of the combination of 1.3 and 0.88 mm data (a zoom-in view), with contours at 6σ, 8σ, and 10σ. The insert cross in the bottom left corner marks the azimuthal angle convention used in this work. Bottom: the azimuthal intensity profile along the B42 ring, obtained as the average emission from 0.″26 to 0.″28 in the disk plane. The clump peak is at 32° and one gray tick indicates 60° separation. The gray shaded region indicates the standard deviation of emission within 200°–360°. The Gaussian profile in the top right corner shows the FWHM of the synthesized beam.

emission), and $\alpha = 1.4$ and $\omega_{\rm smooth} = 0.1$ (to damp high-frequency oscillations in the model brightness profile). We fixed the disk inclination of 50.°2 and position angle to 61°9 (Facchini et al. 2020), and determined phase-center offsets by fitting the ellipse centroid of the bright B69 ring in the image. We estimated $\delta_{\rm RA} = 0.4$ mas and $\delta_{\rm Dec} = 0.2$ mas for B6, and $\delta_{\rm RA} = -1.5$ mas and $\delta_{\rm Dec} = -1.0$ mas for B7.

The images synthesized from the residual visibilities are shown in Figure 3 (the full `frank` fitting results, including the comparison of data and model, are presented in Appendix A). The two nonaxisymmetric emission features are clearly seen along the B42 ring at both wavelengths, at significance levels of 15σ and 8σ for B6 and B7, respectively (the 1σ noise is measured as the rms scatter in an annulus from 4″ to 8″ from the disk center). Considering the images without JvM correction, the excess emission features are detected at 10σ and 6σ for B6 and B7, respectively. Evident residuals are also visible at larger disk radii, which could be due to elevated emission surfaces, mismatches in the geometry properties of individual rings, or perturbations from embedded planets (see also Figure 4). Varying the inclination and position angles by 1° or the center offsets by 3 mas (a half pixel in the image) from the default values produces even more prominent residuals, in particular on large scales. Regardless, in all cases the two asymmetric features in the B42 ring are preserved and stand out. Note that significance of these emission features is evaluated based on rms noise defined in emission-free regions at large scales. If we define the noise level in local regions along the ring (in azimuths > 200°), the clump and arc are also clearly detected at both bands (4σ–5σ).

The clump is unresolved in the residual maps. It has a flux density of ∼0.08 and 0.13 mJy at 1.3 and 0.88 mm, respectively, corresponding to a dust mass of 0.03–0.07 $M_\oplus$ for a dust temperature of 20 K and the DSHARP opacity with a maximum grain size of 1 mm ($\kappa_{1.3\ \rm mm} = 1.9\ \rm cm^2\ g^{-1}$ and $\kappa_{0.88\ \rm mm} = 3.6\ \rm cm^2\ g^{-1}$; Birnstiel et al. 2018). The arc is resolved in 3–4 independent beams along the ring in the azimuthal direction, with integrated fluxes about 4 times higher than the clump.

When comparing the nonaxisymmetric features at the two wavelengths, subtle differences in their locations were identified. The peak position of the B7 clump is offset by 5° clockwise from B6. The offset estimated from the data directly (before model subtraction) is slightly smaller (offset of 4°; see the bottom right panel of Figure 3). This difference can be explained by the fluctuations (or intrinsic asymmetry) along the underlying dust ring. For example, brighter emission is seen to the southwest (smaller azimuthal angle) of the clump in B6 that can cause the shift of the clump peak in the residual map. To test if the offset between the two bands can be caused by CLEAN artifacts, we created mock visibilities by injecting a point source with comparable flux to the clump along the B42 ring in the data (500 samples with randomly assigned azimuthal locations, excluding regions of the excess emission features) and estimated its azimuthal shift in the recovered residual image. In most cases (∼80%), the shift is within 1°. We also explored if the shift could be due to orbital motion. We made images with only the long-baseline executions conducted in 2019 July, and similar offsets were observed. Therefore, this peak shift might reflect a truly different spatial distribution of grains with different sizes. At a semimajor axis of 42 au, a full orbit takes 246.9 yr and the clump will move by $\sim 1.^\circ 5\ \rm yr^{-1}$ counterclockwise if following Keplerian motion. Such movement could be witnessed with new observations taken from now on, given a minimum 3 yr time baseline.

We assigned an azimuthal range of 115°–195° for the arc feature (the azimuthal angle convention is shown in Figure 2), though the edges of this feature are hard to determine. While the B6 residual arc appears more centrally peaked and the B7 one appears more clumpy, quantifying any spatial variations between the two wavelengths is challenging given the low surface brightnesses. Nevertheless, the main body of the arc seems to reside outside the peak of the B42 ring. Possible explanations include a slightly eccentric inner ring and elevated emission surface of the arc.

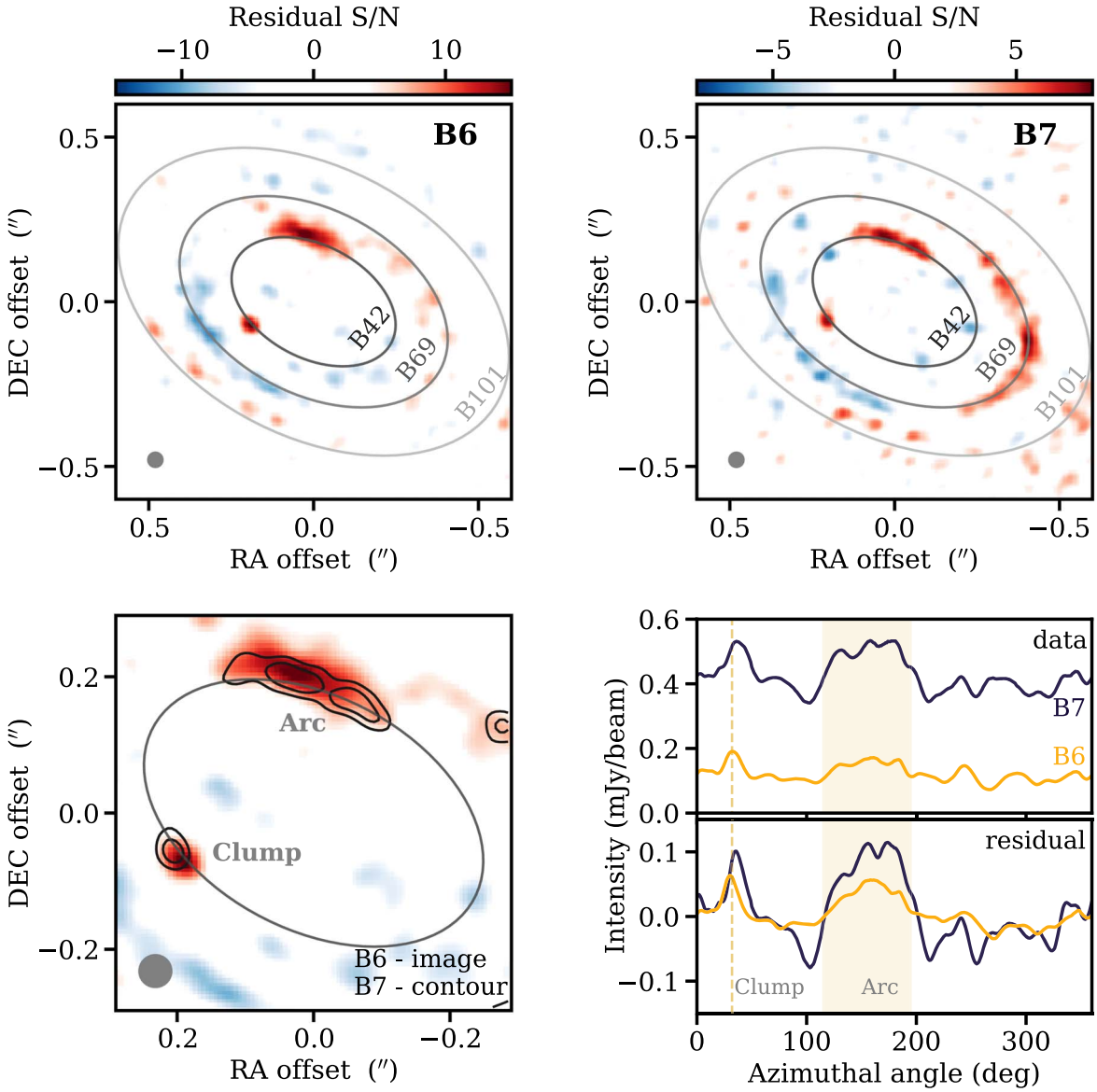

Figure 3. Top panels: residual images after subtracting the `frank` model, shown in signal-to-noise ratio. The images are convolved with the same circular beam of 50 mas, with noise levels of 4.4 and 15.5μJy beam^{-1} at B6 and B7, respectively. The three ellipses indicate the derived ring locations. Bottom left: the zoom-in comparison of the two residual images for the relative locations of the two excess emission features, with B7 residuals shown in contours at 4 and 6σ. Bottom right: the B42 azimuthal intensity profiles from the data (top) and residual images (bottom). The vertical dashed line marks the peak location of the clump identified in the B6 data at 32° and the shaded region is a rough estimate of the arc extension from 115°–195°.

4. Discussion

We have detected nonaxisymmetric dust continuum emission features with a (pointlike) clump and (more extended) arc morphology separated by ∼120° in azimuth along the faint B42 ring in the LkCa 15 disk. These features are robust, as they are seen with high S/N in independent observations at two different wavelengths. Though the flux of the clump is comparable to predictions of CPD emission levels for Jupiter-mass planets (Zhu et al. 2018), the observed azimuthal shift between the B6 and B7 images that could not be accounted for by Keplerian motion makes the possibility that it represents a CPD unlikely. Instead, the fact that the clump and the arc are separated by roughly 120° suggests that the B42 ring may trace dust particles co-orbiting with an embedded planet (in "horseshoe" orbits) with enhanced accumulation in the vicinity of the L_4 and L_5 Lagrangian points.

In the framework of planet–disk interactions, the propagation of density waves creates gaps on both sides of the planet where dust particles are trapped at the gap edges, while a fraction of dust comoves with the planet in a horseshoe-shaped region (e.g., Kley & Nelson 2012; Paardekooper et al. 2022). The dust horseshoe ring has been explored in hydrodynamical simulations (e.g., Dong et al. 2017; Ricci et al. 2018), and has been advocated as an explanation for certain ALMA observations (e.g., HL Tau, Dipierro et al. 2015; HD 169142, Pérez et al. 2019). The morphology of the horseshoe ring depends on many disk and planet properties, including the degree of dust–gas coupling, disk viscosity, local thermodynamics (i.e., scale height aspect ratio h/r), and planet mass, among others.

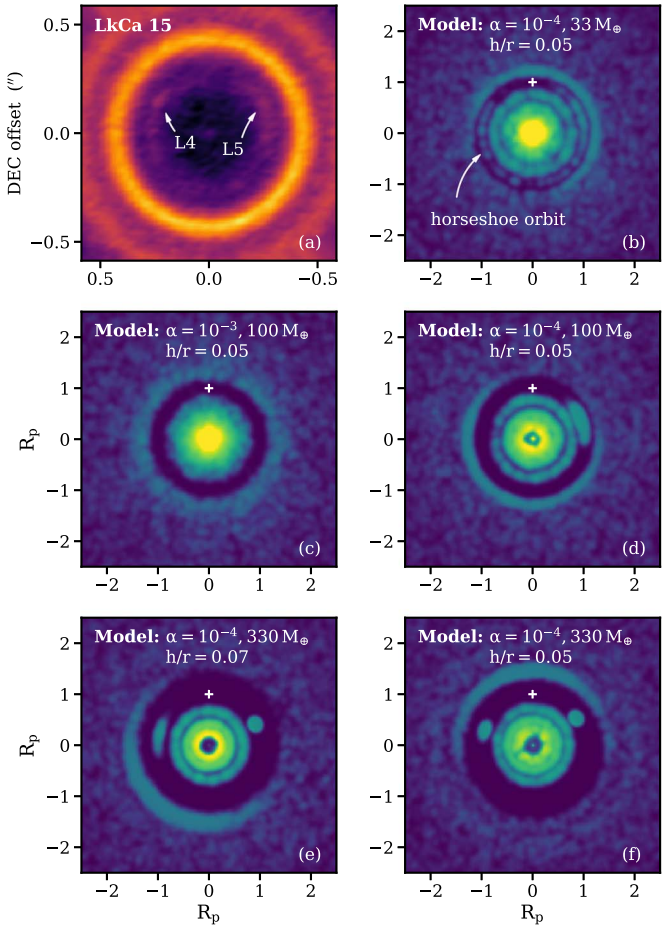

Figure 4. Panel (a): the deprojected 1.1 mm (B6+B7 combined) image of the LkCa 15 disk, with the L_4 and L_5 points marked. Panels (b)–(f): 1.3 mm continuum images from planet–disk interaction models selected from Zhang et al. (2018), assuming the maximum grain size of 1 mm. In each panel, the planet is located at (0, 1) and marked with a "+" symbol; it orbits in the counterclockwise direction, following the L_4/L_5 annotation in panel (a).

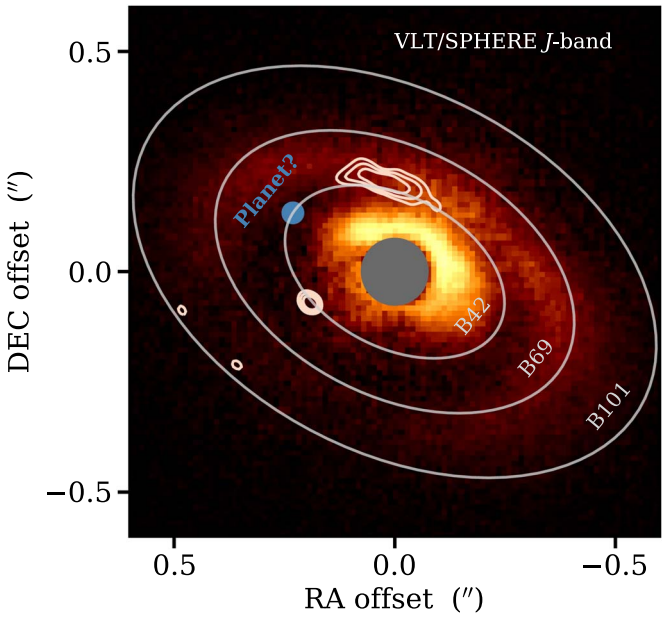

Figure 5. The comparison of near-IR dust scattered light (SPHERE IRDIS J-band imaging polarimeter; Thalmann et al. 2016) and ALMA millimeter dust rings (the three gray ellipses) in the LkCa 15 disk. The inner working angle of 80 mas in the SPHERE image is masked out. The ALMA B6 residual contours are shown at 8σ, 10σ, and 12σ levels in pink. The putative planet location is indicated.

Figure 4 illustrates some of the key dependencies using a subset of the 2D hydrodynamical models[12] calculated by Zhang et al. (2018). Higher viscosity (characterized by the α parameter, panels (c) and (d)) tends to destroy the horseshoe ring, as diffusion smooths out the gas density perturbations (see also Rodenkirch et al. 2021). More massive planets generate stronger nonaxisymmetric features, with higher dust concentration around the Lagrangian points (panels (b), (d), and (f)).

Our observations of the B42 dust ring in the LkCa 15 disk best resemble the scenario where a Neptune-mass planet is perturbing a low-viscosity disk (panels (a) and (b) in Figure 4). Based on the gas emission morphology (Öberg et al. 2010; Jin et al. 2019 separating front and back disk sides), the disk around LkCa 15 rotates counterclockwise. Therefore, the clump and arc features are likely marking dust associated with the leading (L_4) and trailing (L_5) Lagrangian points, respectively.

Montesinos et al. (2020) explored the evolution of dust around Lagrangian points when the disk is shaped by interactions with a planet and suggested that L_4 and L_5 can act as dust traps. However, they found the dust concentration at Lagrangian points is highly dynamic, with morphologies quickly evolving with time. In addition, multiple physical processes (e.g., drag forces, grain collisions and growth) could modify these dust distributions, resulting in different emission morphologies (e.g., dust feedback can lead to fragmentation of the dust clump; Rodenkirch et al. 2021). Therefore, the clump and arc morphologies in the B42 ring may be transient: using them to infer the planet and disk properties is not trivial.

The shift of the clump peak that was discussed in Section 3.2 was also predicted by Rodenkirch et al. (2021), when modeling the HD 163296 disk. They found that smaller grains with lower Stokes number around L_4 are located closer to the planet (see their Figures 8 and 9). The brighter emission in the arc is also consistent with their prediction that larger grains are preferentially trapped at the L_5 point. The accumulation of dust particles in the vicinity of Lagrangian points may trigger the formation of Trojan asteroids or even Earth-mass bodies around massive planets (e.g., Lyra et al. 2009). The estimated dust mass in the clump and arc is sufficient to account for the Jovian Trojans in our solar system, though slightly more Trojans are found around L_4 (Vinogradova & Chernetenko 2015), in contrast with our inference of more dust mass in L_5.

Based on the identification of the clump (L_4) and the arc (L_5), we can infer that the putative planet location along the B42 ring is roughly aligned with the major axis of the LkCa 15 disk to the northeast as indicated in Figure 5. Along the ring, it is interesting that the vicinity of the planet is comparatively depleted of dust emission in the ALMA data (see Figure 2). As we are interested in localized emission within the horseshoe ring, we estimate the noise level from the standard deviation along the B42 ring (from azimuths >200°) and find a 3σ upper limit of $\sim$70 μJy at 0.88 mm ($\sim$33 μJy at 1.3 mm) for any associated CPD, which translates into a dust mass upper limit of 0.02–0.03 $M_\oplus$ following the same assumptions as in Section 3.2. This is a bit higher than the emission levels seen from the planet PDS 70 c (46 μJy; Benisty et al. 2021) and

[12] CPDs were not included in these simulations, as dust evolution in CPDs has not been well understood. Given the small scale of a CPD, its influence on dust evolution in the horseshoe region should be minimal.

planetary-mass object SR 12 c (63 μJy; Wu et al. 2022) at 0.88 mm, when normalized to the LkCa 15 distance. Deeper ALMA observations are needed to put comparable constraints on the presence of a CPD in the LkCa 15 disk.

For disks with inner cavities, the masses of perturbers are hard to constrain because the gap width opened by each perturber is largely unknown. In the case of LkCa 15, gap width associated with the B42 planet can be estimated based on locations of the horseshoe ring and the adjacent outer ring (B69), following the definition in Zhang et al. (2018). Assuming canonical disk conditions of $h/r = 0.05$, $\alpha = 10^{-4}$, and a maximum grain size of 1 mm, a fractional gap width of 0.52 corresponds to a planet mass of 0.1–0.3 $M_{\rm Jup}$ (Figure 12 in Zhang et al. 2018; see also Bae et al. 2017), which is below the current detection limit from direct imaging for LkCa 15 at 42 au (Asensio-Torres et al. 2021).

Additional constraints on the planet properties can be made by comparing different disk tracers. Interestingly, the gap seen in the near-IR scattered-light image (Thalmann et al. 2016) shown in Figure 5 is coincident with the planet horseshoe ring identified from the millimeter dust emission. The absence of scattered light is likely due to inner disk shadowing for this low dust surface density area. Based on the gap morphology in the scattered light, Dong & Fung (2017) predicted a planet mass of 0.15 $M_{\rm Jup}$ (1.5 $M_{\rm Jup}$) for $\alpha = 10^{-4}$ ($\alpha = 10^{-2}$) at 42 au with hydrodynamic simulations. The presence of material along the horseshoe orbit from the ALMA data presented here would prefer the lower-planet-mass scenario. As a higher-mass planet would more effectively prevent gas flowing through the cavity, this low-mass scenario is also more consistent with the presence of substantial amounts of molecular gas in the inner LkCa 15 disk (Leemker et al. 2022). Nevertheless, this B42 planet may not be sufficient to fully account for both the wide inner cavity and the B101 ring further out, where additional planets and/or other mechanisms might act in concert to shape the LkCa 15 disk.

Though we favor this Lagrangian-point dust-trapping scenario for dust emission around 42 au as it explains the clump and arc features simultaneously, there are also other possibilities. The arc could be part of a spiral arm (e.g., Andrews et al. 2021), which might explain its radial offset from the ring center. Both the arc and clump could be vortices, for which gas kinematics that traces the anticyclonic motion will help identify their nature (Boehler et al. 2021). Meanwhile, searching for gas kinematic perturbations near the predicted location of the B42 planet would be especially compelling to test our proposed scenario.

5. Summary

In this Letter, we reported a detailed investigation of high-quality ALMA continuum observations of newly identified dust features in the LkCa 15 disk. We found that the continuum emission ring at a radius of 42 au looks very similar to the horseshoe ring produced in planet–disk interaction models. We postulated that the two robustly detected nonaxisymmetric emission features along this ring with a separation of $\sim$120° mark dust concentrations at the L_4 and L_5 Lagrangian points, which are consistent with hydrodynamic model predictions for interactions with an embedded $\sim$Neptune-mass planet. Multiple additional lines of evidence, including dust trapping in a ring at 69 au and the fact that the 42 au ring coincides with a gap in the near-IR scattered light, also support the scenario of an embedded planet. This putative planet should be located at a projected separation of 0.″27 from the star with a position angle of $\sim$60° (roughly aligned with the disk major axis). However, no pointlike CPD emission is identified, with a 3σ upper limit of $\sim$70 μJy at 0.88 mm ($\sim$33 μJy at 1.3 mm) along the ring.

These results demonstrate the utility of deep high-resolution ALMA images in revealing the faint, subtle features predicted by hydrodynamic simulations. These features provide compelling new evidence of ongoing planet formation in structured disks and offer a new avenue for guiding planet searches.

We thank the referees for their helpful comments that improved the clarity of this manuscript. F.L. is grateful to Gregory Herczeg, Rixin Li, and Yifan Zhou for support. F.L. acknowledges support from the Smithsonian Institution as the Submillimeter Array (SMA) Fellow. F.L. and S.A. acknowledge funding support from the National Aeronautics and Space Administration under grant No. 17-XRP17_2-0012 issued through the Exoplanets Research Program. A.I. acknowledges support from the National Aeronautics and Space Administration under grant No. 80NSSC18K0828. Support for J.H. was provided by NASA through the NASA Hubble Fellowship grant #HST-HF2-51460.001-A awarded by the Space Telescope Science Institute, which is operated by the Association of Universities for Research in Astronomy, Inc., for NASA, under contract NAS5-26555. S.Z. and Z.Z. acknowledge support from NASA through the NASA FINNEST grant 80NSSC20K1376. Z.Z. acknowledges support from the National Science Foundation under CAREER grant AST-1753168. This project has received funding from the European Research Council (ERC) under the European Unions Horizon 2020 research and innovation program (PROTOPLANETS, grant agreement No. 101002188).

This Letter makes use of the following ALMA data sets: 2012.1.00870.S, 2015.1.00118.S, 2018.1.00945.S, 2018.1.01255.S, and 2018.1.00350.S. ALMA is a partnership of ESO (representing its member states), NSF (USA), and NINS (Japan), together with NRC (Canada), MOST and ASIAA (Taiwan), and KASI (Republic of Korea), in cooperation with the Republic of Chile. The Joint ALMA Observatory is operated by ESO, AUI/NRAO, and NAOJ. The National Radio Astronomy Observatory is a facility of the National Science Foundation operated under cooperative agreement by Associated Universities, Inc.

Facilities: ALMA, VLT(SPHERE).

Software: analysisUtils (https://casaguides.nrao.edu/index.php/Analysis_Utilities), AstroPy (Astropy Collaboration et al. 2018), CASA (McMullin et al. 2007), frank (Jennings et al. 2020), matplotlib (Hunter 2007), Scipy (Virtanen et al. 2020).

Appendix A
Frank Fitting Results

Figure 6 compares the LkCa 15 ALMA data at B6 and B7 with their corresponding models obtained from `frank` fitting, in both the visibility profile and image plane. The model and residual images are constructed with identical parameters in the `tclean` task as for the data. As seen from the residual map, millimeter emission in the LkCa 15 disk can be broadly described by an axisymmetric model.

The model brightness profiles are shown in Figure 7, and properties of the three prominent dust rings are summarized in Table 2, each described by a Gaussian profile. Rings at the

Table 2
Dust Ring Properties from Frank Fitting

Band	A_{B42} (log Jy Sr^{-1})	r_{B42} (arcsec)	σ_{B42} (arcsec)	A_{B69} (log Jy Sr^{-1})	r_{B69} (arcsec)	σ_{B69} (arcsec)	A_{B101} (log Jy Sr^{-1})	r_{B101} (arcsec)	σ_{B101} (arcsec)
(1)	(2)	(3)	(4)	(5)	(6)	(7)	(8)	(9)	(10)
B6	9.34 ± 0.01	0.266 ± 0.001	0.033 ± 0.001	10.04 ± 0.01	0.435 ± 0.001	0.043 ± 0.001	9.75 ± 0.01	0.638 ± 0.001	0.068 ± 0.001
B7	9.81 ± 0.02	0.269 ± 0.004	0.064 ± 0.007	10.28 ± 0.01	0.430 ± 0.001	0.050 ± 0.001	10.09 ± 0.01	0.629 ± 0.002	0.107 ± 0.003

Note. Column (1): ALMA band. Columns (2)–(4): the fitted amplitude, location, and Gaussian sigma for the B42 ring. Columns (5)–(7): for the B69 ring. Columns (8)–(10): for the B101 ring.

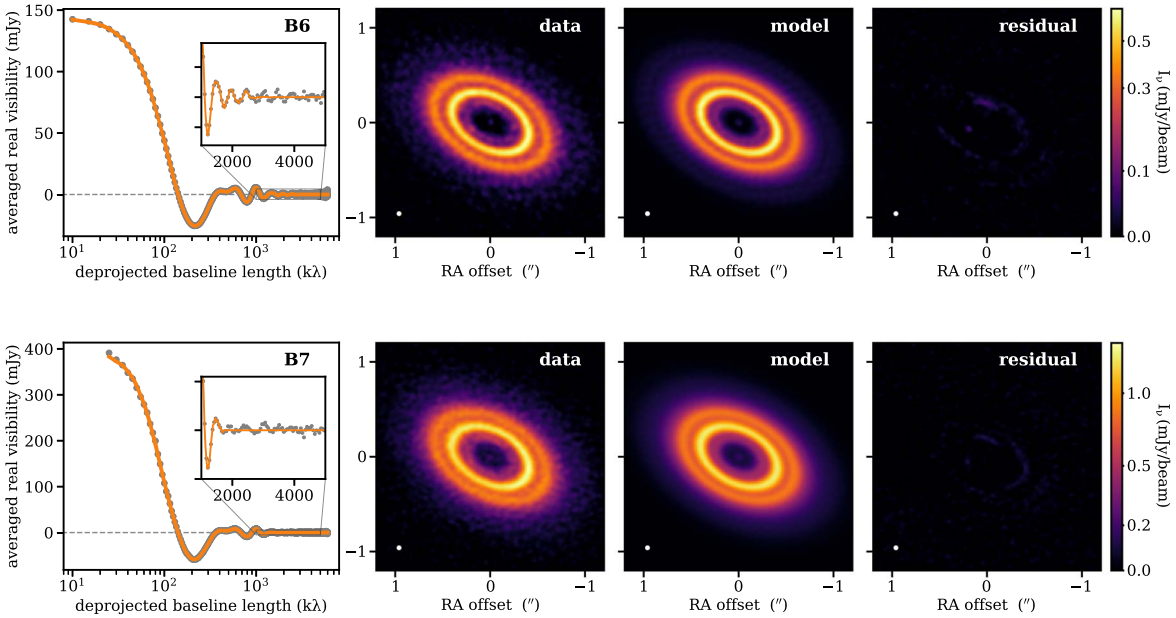

Figure 6. Comparisons of the data and frank model in the visibility profile and image plane for B6 (top panels) and B7 (bottom panels). The data visibilities are binned in 5 $k\lambda$ shown in gray points. The insert panel shows a zoom-in view of the long-baseline part outward of 1 Mλ with data binned in 50 $k\lambda$.

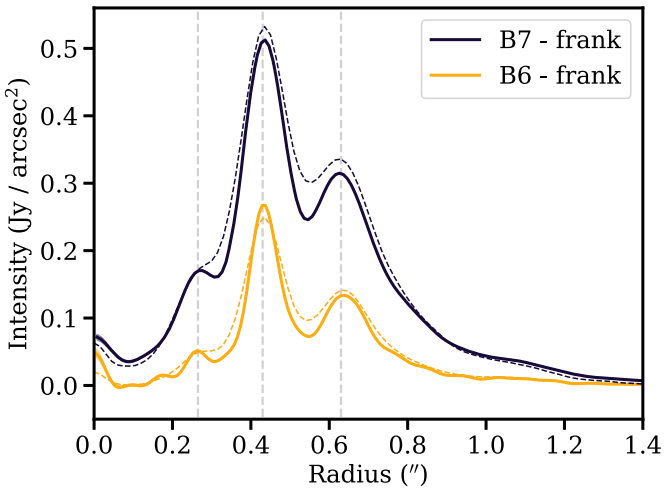

Figure 7. The model brightness profiles derived with `frank`, using the parameters described in Section 3. The three prominent dust rings are marked with the gray vertical lines. The data radial profiles from images convolved with a 50 mas beam are shown in dashed lines for comparison.

longer wavelength of 1.3 mm are generally narrower. The notable difference of the width in the B42 ring is mainly subject to the retrieval of an additional emission component in B6 (around 0.″18). Beyond the three dust rings, the outer disk is associated with a broad emission halo, extending to at least 1.″2 as seen from the B7 profile.

Appendix B
Image Gallery

To assess how angular resolution may affect the recovery of the clump and arc features, we created a set of new images using different combinations of robust weighting parameters and uvtaper in `tclean`. The images, as well as their corresponding `frank` residual maps, are shown in Figure 8, spanning a range of beam sizes from 30 to 90 mas. Except for the extreme case of 30 mas where the B42 ring itself is only marginally detected, the two excess emission features are always clearly identified. However, with a large beam of 90 mas, the B42 ring would be largely unresolved; thus, the retrieval of feature properties (e.g., amplitude, shape) can be highly uncertain. The detection of the two features is also robust when only using the long-baseline configuration data, as shown in the bottom rows of Figure 8.

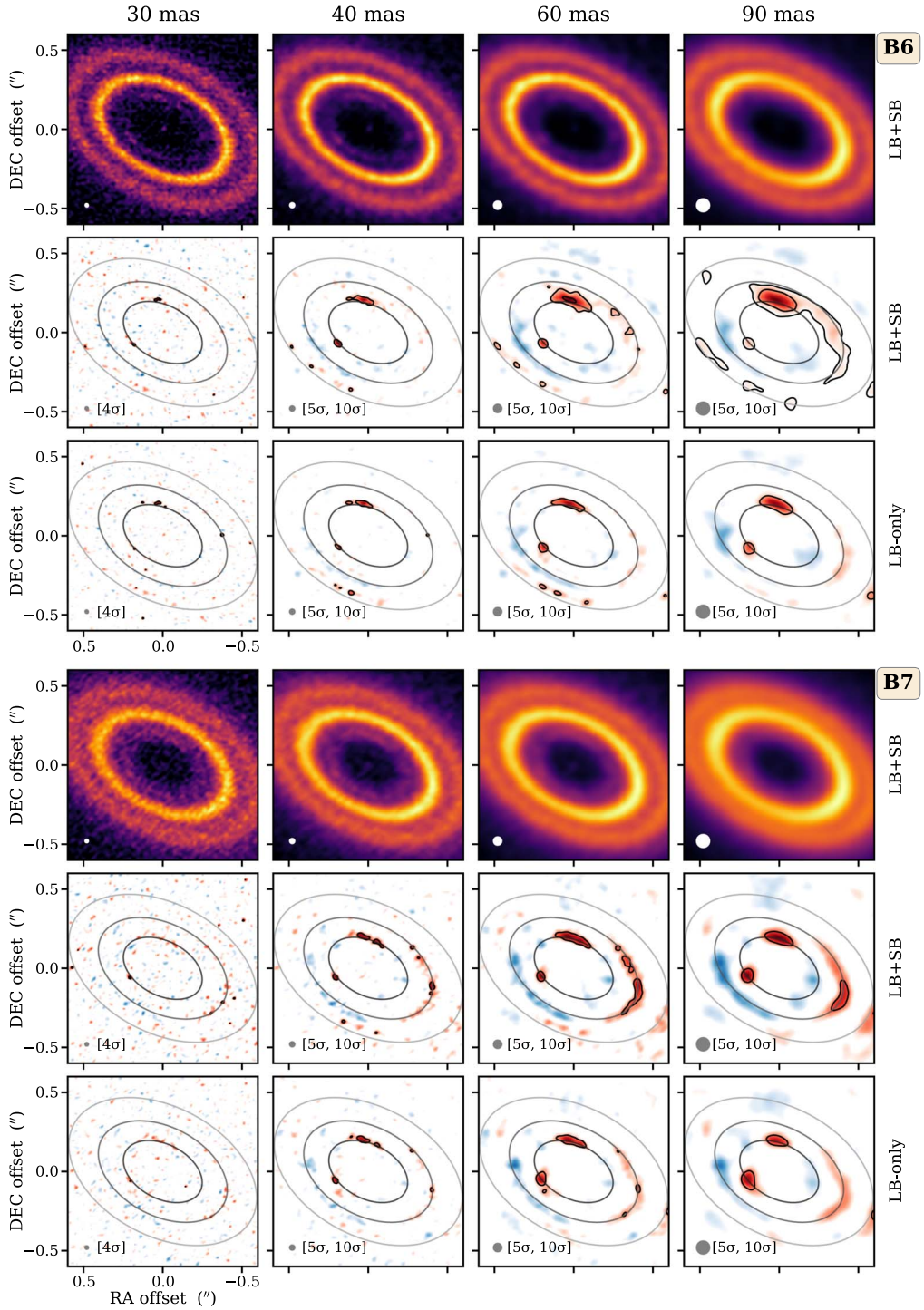

Figure 8. The disk continuum images and `frank` residual maps with different synthesized beams for both B6 (top panels) and B7 (bottom panels). Columns correspond to different beam sizes, as indicated in the top panels. The disk images and first row of residual maps were created with the full combined data, while the second row used only the long-baseline data sets.

ORCID iDs

Feng Long (龙 凤) https://orcid.org/0000-0002-7607-719X
Sean M. Andrews https://orcid.org/0000-0003-2253-2270
Shangjia Zhang (张尚嘉) https://orcid.org/0000-0002-8537-9114
Chunhua Qi https://orcid.org/0000-0001-8642-1786
Myriam Benisty https://orcid.org/0000-0002-7695-7605
Stefano Facchini https://orcid.org/0000-0003-4689-2684
Andrea Isella https://orcid.org/0000-0001-8061-2207
David J. Wilner https://orcid.org/0000-0003-1526-7587
Jaehan Bae https://orcid.org/0000-0001-7258-770X
Jane Huang https://orcid.org/0000-0001-6947-6072
Ryan A. Loomis https://orcid.org/0000-0002-8932-1219
Karin I. Öberg https://orcid.org/0000-0001-8798-1347
Zhaohuan Zhu (朱照寰) https://orcid.org/0000-0003-3616-6822

References

Andrews, S. M. 2020, ARA&A, 58, 483
Andrews, S. M., Elder, W., Zhang, S., et al. 2021, ApJ, 916, 51
Andrews, S. M., Rosenfeld, K. A., Wilner, D. J., & Bremer, M. 2011, ApJL, 742, L5
Asensio-Torres, R., Henning, T., Cantalloube, F., et al. 2021, A&A, 652, A101
Astropy Collaboration, Price-Whelan, A. M., Sipőcz, B. M., et al. 2018, AJ, 156, 123
Bae, J., Pinilla, P., & Birnstiel, T. 2018, ApJL, 864, L26
Bae, J., Teague, R., Andrews, S. M., et al. 2022, ApJL, 934, L20
Bae, J., Zhu, Z., & Hartmann, L. 2017, ApJ, 850, 201
Benisty, M., Bae, J., Facchini, S., et al. 2021, ApJL, 916, L2
Benisty, M., Dominik, C., Follette, K., et al. 2022, arXiv:2203.09991
Birnstiel, T., Dullemond, C. P., Zhu, Z., et al. 2018, ApJL, 869, L45
Blakely, D., Francis, L., Johnstone, D., et al. 2022, ApJ, 931, 3
Boehler, Y., Ménard, F., Robert, C. M. T., et al. 2021, A&A, 650, A59
Brittain, S. D., Najita, J. R., Dong, R., & Zhu, Z. 2020, ApJ, 895, 48
Currie, T., Lawson, K., Schneider, G., et al. 2022, NatAs, 6, 751
Currie, T., Marois, C., Cieza, L., et al. 2019, ApJL, 877, L3
Czekala, I., Loomis, R. A., Teague, R., et al. 2021, ApJS, 257, 2
Dipierro, G., Price, D., Laibe, G., et al. 2015, MNRAS, 453, L73
Donati, J.-F., Bouvier, J., Alencar, S. H., et al. 2019, MNRAS, 483, L1
Dong, R., & Fung, J. 2017, ApJ, 835, 146
Dong, R., Li, S., Chiang, E., & Li, H. 2017, ApJ, 843, 127
Facchini, S., Benisty, M., Bae, J., et al. 2020, A&A, 639, A121
Gaia Collaboration, Brown, A. G. A., Vallenari, A., et al. 2018, A&A, 616, A1
Hunter, J. D. 2007, CSE, 9, 90
Isella, A., Benisty, M., Teague, R., et al. 2019, ApJL, 879, L25
Isella, A., Chandler, C. J., Carpenter, J. M., Pérez, L. M., & Ricci, L. 2014, ApJ, 788, 129
Jennings, J., Booth, R. A., Tazzari, M., Clarke, C. J., & Rosotti, G. P. 2022, MNRAS, 509, 2780
Jennings, J., Booth, R. A., Tazzari, M., Rosotti, G. P., & Clarke, C. J. 2020, MNRAS, 495, 3209
Jin, S., Isella, A., Huang, P., et al. 2019, ApJ, 881, 108
Jorsater, S., & van Moorsel, G. A. 1995, AJ, 110, 2037
Keppler, M., Benisty, M., Müller, A., et al. 2018, A&A, 617, A44
Kley, W., & Nelson, R. P. 2012, ARA&A, 50, 211
Kraus, A. L., & Ireland, M. J. 2012, ApJ, 745, 5
Leemker, M., Booth, A. S., van Dishoeck, E. F., et al. 2022, A&A, 663, A23
Lodato, G., Dipierro, G., Ragusa, E., et al. 2019, MNRAS, 486, 453
Long, F., Pinilla, P., Herczeg, G. J., et al. 2020, ApJ, 898, 36
Lyra, W., Johansen, A., Klahr, H., & Piskunov, N. 2009, A&A, 493, 1125
McMullin, J. P., Waters, B., Schiebel, D., Young, W., & Golap, K. 2007, in ASP Conf. Ser. 376, Astronomical Data Analysis Software and Systems XVI, ed. R. A. Shaw, F. Hill, & D. J. Bell (San Francisco, CA: ASP), 127
Montesinos, M., Garrido-Deutelmoser, J., Olofsson, J., et al. 2020, A&A, 642, A224
Öberg, K. I., Qi, C., Fogel, J. K. J., et al. 2010, ApJ, 720, 480
Paardekooper, S.-J., Dong, R., Duffell, P., et al. 2022, arXiv:2203.09595
Pérez, S., Casassus, S., Baruteau, C., et al. 2019, AJ, 158, 15
Piétu, V., Dutrey, A., Guilloteau, S., Chapillon, E., & Pety, J. 2006, A&A, 460, L43
Pinilla, P., Benisty, M., & Birnstiel, T. 2012, A&A, 545, A81
Pinilla, P., van der Marel, N., Pérez, L. M., et al. 2015, A&A, 584, A16
Pinte, C., Teague, R., Flaherty, K., et al. 2022, arXiv:2203.09528
Rau, U., & Cornwell, T. J. 2011, A&A, 532, A71
Ricci, L., Liu, S.-F., Isella, A., & Li, H. 2018, ApJ, 853, 110
Rodenkirch, P. J., Rometsch, T., Dullemond, C. P., Weber, P., & Kley, W. 2021, A&A, 647, A174
Sallum, S., Follette, K. B., Eisner, J. A., et al. 2015, Natur, 527, 342
Thalmann, C., Janson, M., Garufi, A., et al. 2016, ApJL, 828, L17
Vinogradova, T. A., & Chernetenko, Y. 2015, SoSyR, 49, 391
Virtanen, P., Gommers, R., Oliphant, T. E., et al. 2020, NatMe, 17, 261
Wu, Y.-L., Bowler, B. P., Sheehan, P. D., et al. 2022, ApJL, 930, L3
Zhang, S., Zhu, Z., Huang, J., et al. 2018, ApJL, 869, L47
Zhu, Z., Andrews, S. M., & Isella, A. 2018, MNRAS, 479, 1850
Zhu, Z., Nelson, R. P., Hartmann, L., Espaillat, C., & Calvet, N. 2011, ApJ, 729, 47